Numerical Optimization of the Dirichlet Boundary Condition in the Phase Field Model with an Application to Pure Substance Solidification

Aleš Wodecki · **Pavel Strachota** · **Tomáš Oberhuber** · **Kateřina Škardová** · **Monika Balázsová**

Abstract As opposed to the distributed control of parabolic PDE's, very few contributions currently exist pertaining to the Dirichlet boundary condition control for parabolic PDE's. This motivates our interest in the Dirichlet boundary condition control for the phase field model describing the solidification of a pure substance from a supercooled melt. In particular, our aim is to control the time evolution of the temperature field on the boundary of the computational domain in order to achieve the prescribed shape of the crystal at the given time. To obtain efficient means of computing the gradient of the cost functional, we derive the adjoint problem formally. The gradient is then used to perform gradient descent. The viability of the proposed optimization method is supported by several numerical experiments performed in one and two spatial dimensions. Among other things, these experiments show that a linear reaction term in the phase field equation proves to be insufficient in certain scenarios and so an alternative reaction term is considered to improve the models behavior.

————————————————

A. Wodecki
Department of Mathematics, Faculty of Nuclear Sciences and Physical Engineering, Czech Technical University in Prague
Tel.: +420-733-522-679
E-mail: wodecale@fjfi.cvut.cz

P. Strachota
Department of Mathematics, Faculty of Nuclear Sciences and Physical Engineering, Czech Technical University in Prague
Tel.: +420-22435-8563
E-mail: pavel.strachota@fjfi.cvut.cz

T. Oberhuber, K. Škardová, M. Balázsová
Department of Mathematics, Faculty of Nuclear Sciences and Physical Engineering, Czech Technical University in Prague
E-mail: tomas.oberhuber@fjfi.cvut.cz, katerina.skardova@fjfi.cvut.cz

1 Introduction

Phase field models have found utility in various areas including phase transition modeling [5, 14, 22, 25], multi component flow simulations [2, 3] and fracture mechanics [10, 29]. They can take the form of an initial boundary-value problem for a system of partial differential equations (PDE's). In this case, one of the PDE's is the phase field equation, which is derived by the minimization of the Allen-Cahn or Cahn-Hilliard functional [1, 9]. To describe the solidification of a pure supercooled liquid [7, 28] the phase equation is augmented by the heat equation. This formulation is linked to materials science and practical applications, where controlling solidification is of interest [4, 18, 21, 27].

The optimal control phase field models (PFM) has been studied extensively both from a theoretical and numerical simulations perspective. In particular, the distributed control of this type of PFM with homogeneous Neumann or Dirichlet boundary conditions has been addressed by a large number of publications [12, 13, 20, 30]. Another type of control that may be considered for PFM is the Neumann or Robin Control (NoR) [11, 15]. To the authors' best knowledge however, the Dirichlet boundary control of parabolic equations has not been studied as extensively. Hinze et. al. [16] and Kunisch [24] have utilized the very weak formulation to derive optimality conditions and perform calculations using the finite element method (FEM) [16, 24]. More recently, Gudi et. al. have utilized the weak formulation along with an alternative control space formulation to derive theoretical results and perform FEM simulations as well [17]. All these contributions however, only address a single parabolic PDE and do not apply to the optimization of the Dirichlet boundary condition in the PFM.

In this article, the numerical optimization of the Dirichlet boundary condition in a PFM that describes the solidification of a supercooled pure substance is discussed. Since we restrict ourselves to numerical simulations, the strong form can be used to formally derive the adjoint equations. These are then used to propose an efficient method of gradient computation. Gradient descent is then performed using an initial guess to eventually arrive at a locally optimal control. A number of numerical simulations in one and two dimensions have been performed to show the effectiveness of this method (see Section 5). Some of these simulations show that the optimization is quantitatively and qualitatively affected by the inadequacies of the linear reaction term in the phase field equation (see Section 5.1.3). An alternative reaction term, proposed in [28], is then used to remove these limitations.

2 General Problem Formulation and Gradient Computation

For the general theory, we formally follow [19]. Let Y, U be Banach spaces and Z be a Hilbert space. We call Y the solution space and U the control space. Consider a map

$$e : Y \times U \to Z.$$

We call e the state map, implicitly defining the dependence of the solution $y \in Y$ on the control $u \in U$ by the state equation

$$e(y, u) = 0. \tag{1}$$

For example, the state equation can assume the form of a system of ordinary differential equations (ODE's) with boundary conditions or a system of PDE's with boundary and initial conditions. In this setting, u is involved in the formulation of the problem for the ODE's or

PDE's and y represents its solution. In particular, u can appear in the source term or an initial or boundary condition.

Assume that there exists a map $S : U \to Y$ such that

$$e(S(u),u) = 0.$$

We call S the solution operator. The existence of the map S is equivalent to the existence and uniqueness of the solution $y = S(u)$ of (1) for any control $u \in U$.

We introduce the cost functional $J : Y \times U \to \mathbb{R}$. The fundamental minimization problem then reads

$$\min_{u \in U} J(y,u) \tag{2}$$

$$\text{s.t. } e(y,u) = 0 \text{ where } y \in Y, u \in U. \tag{3}$$

To obtain the derivative of the cost functional J with respect to u, it is possible to either perform direct computation (sensitivity analysis) or use adjoint methods [19]. We opt for the latter approach since it's computationally more efficient when performing optimization with respect to a large amount of parameters.

First, define the reduced cost functional associated to the fundamental problem (2)-(3) as

$$\hat{J}(u) = J(y(u),u),$$

where the term $y(u)$ is used in place of $S(u)$ to denote the solution y of the state equation (1) for the given control u. Then the fundamental problem (2)-(3) simply becomes

$$\min_{u \in U} \hat{J}(u). \tag{4}$$

We compute the Fréchet derivative of $\hat{J}$ at u formally. Define the Lagrange function $L : Y \times U \times Z \to \mathbb{R}$ as

$$L(y,u,\lambda) \equiv J(y,u) + \langle \lambda, e(y,u) \rangle_Z, \tag{5}$$

where λ is called the adjoint variable. We notice that since $e(y(u),u) = 0$ for all $u \in U$, we have

$$L(y(u),u,\lambda) = \hat{J}(u). \tag{6}$$

By differentiating (6), we arrive at

$$\hat{J}'(u)s = L_y(y(u),u,\lambda)y'(u)s + L_u(y(u),u,\lambda)s, \tag{7}$$

where $s \in U$. The equation

$$L_y(y(u),u,\lambda) = 0 \tag{8}$$

is called the adjoint problem. Finding a particular $\lambda_0 \in Z$ that solves (8) leads to a simplified calculation of the derivative (7) and we no longer need to compute $y'(u)$ in order to evaluate $\hat{J}'(u)s$ for a given direction $s \in U$.

3 Adjoint Problem for Optimizing the Solution of the Phase Field Problem

Using strong formalism, the procedure shown in Section 2 is applied to an optimization problem where the state equation (3) is the isotropic phase field problem in a simplified dimensionless form [6, 7, 8, 28]. Let $\Omega \subset \mathbb{R}^n$ be a bounded domain and let $T > 0$. The course of solidification (or melting) of a pure material in Ω is described by the evolution of the phase field $\tilde{y}$ with values between 0 and 1, identifying the solid subdomain $\Omega_s(t)$, the liquid subdomain $\Omega_l(t)$ and the phase interface $\Gamma(t)$ by

$$\Omega_s(t) = \left\{ x \in \Omega; \tilde{y}(t,x) > \frac{1}{2} \right\}, \tag{9}$$

$$\Omega_l(t) = \left\{ x \in \Omega; \tilde{y}(t,x) < \frac{1}{2} \right\}, \tag{10}$$

$$\Gamma(t) = \left\{ x \in \Omega; \tilde{y}(t,x) = \frac{1}{2} \right\}. \tag{11}$$

The phase field problem governs the evolution of both the phase field $\tilde{y}$ and the temperature field y by modeling phase transitions and heat transfer inside Ω. Our aim is to obtain such solution that approaches the prescribed crystal shape at the given time T (i.e., the shape of the solid subdomain $\Omega_s(T)$). This is done by controlling the time-dependent Dirichlet boundary condition for the temperature y.

Consider the problem

$$\min_{u \in U} J(y, \tilde{y}, u) \equiv \frac{1}{2} \int_{\Omega} \left| \tilde{y}(T,x) - \tilde{y}_f(x) \right|^2 \mathrm{d}x + \frac{\alpha}{2} \int_0^T \int_{\partial\Omega} |u(t,x)|^2 \, \mathrm{d}S \mathrm{d}t \tag{12}$$

s.t.

$$\begin{align}
y_t &= \Delta y + H \tilde{y}_t, & \text{in } (0,T) \times \Omega, \tag{13}\\
y|_{\partial\Omega} &= u & \text{on } [0,T] \times \partial\Omega, \tag{14}\\
y|_{t=0} &= y_{\mathrm{ini}} & \text{in } \Omega, \tag{15}\\
\gamma \xi^2 \tilde{y}_t &= \xi^2 \Delta \tilde{y} + f_0(y, \tilde{y}; \xi) & \text{in } (0,T) \times \Omega, \tag{16}\\
\tilde{y}|_{\partial\Omega} &= \tilde{y}_{\mathrm{bc}} & \text{on } [0,T] \times \partial\Omega, \tag{17}\\
\tilde{y}|_{t=0} &= \tilde{y}_{\mathrm{ini}} & \text{in } \Omega, \tag{18}
\end{align}$$

where $\tilde{y}_f \in \mathrm{L}^2(\Omega)$ in (12) is the target profile of the phase field $\tilde{y}$, α denotes the strength of the regularization term, and

$$f_0(y, \tilde{y}; \xi) = \tilde{y}(1 - \tilde{y})\left(\tilde{y} - \frac{1}{2}\right) - \beta \xi (y - y_{\mathrm{mt}}). \tag{19}$$

Equation (13) is the heat equation with release of the latent heat of fusion H. The corresponding Dirichlet boundary condition for the temperature y is given by the control $u \in \mathrm{C}([0,T] \times \partial\Omega)$ and the initial temperature field is determined by (15).

Next, (16) is the Allen-Cahn (phase field) equation with a simple linear form of the reaction term [23, 28], containing the melting temperature y_{mt}, the parameter ξ related to the interface thickness, and the dimensionless model parameters γ, β. For simplicity, we consider a constant Dirichlet boundary condition (17) for $\tilde{y}$. Finally, the initial condition (18) describes the initial shape of the crystal $\Omega_s(0)$.

In order for the phase interface to form correctly and the solution to have physical interpretation, the reaction term on the right hand side of (16) must have three roots in terms of $\tilde{y}$ and thus satisfy the condition

$$\beta \xi \left(y - y_{\mathrm{mt}} \right) \in \left(-\frac{\sqrt{3}}{36}, \frac{\sqrt{3}}{36} \right), \tag{20}$$

as detailed in [7, 8, 28]. As will be shown further in Section 5, the presented formulation of the optimization problem may yield the optimal control u such that the solution $(y, \tilde{y})$ violates (20).

Let us proceed to the derivation of the adjoint problem. Consider the setting:

- $Y \equiv \mathrm{C}^2 \left([0, T] \times \overline{\Omega} \right)^2$,
- $U \equiv \mathrm{C} \left(\partial \Omega \times [0, T] \right)$,
- $Z \equiv \mathrm{L}^2 \left([0, T] \times \overline{\Omega} \right)^2 \times \mathrm{L}^2 \left(\partial \Omega \times [0, T] \right)^2 \times \mathrm{L}^2 \left(\Omega \right)^2$.

Define the state equation operator component-wise as

$$\begin{aligned}
e^1 (y, \tilde{y}) &= y_t - \Delta y - H \tilde{y}_t, \\
e^2 (y, u) &= y|_{t=0} - y_{\mathrm{ini}}, \\
e^3 (y) &= y|_{\partial \Omega} - u, \\
e^4 (y, \tilde{y}) &= \gamma \xi^2 \tilde{y}_t - \xi^2 \Delta \tilde{y} - \tilde{y} (1 - \tilde{y}) \left(\tilde{y} - \frac{1}{2} \right) + \beta \xi \left(y - y_{\mathrm{mt}} \right), \\
e^5 (\tilde{y}) &= \tilde{y}|_{t=0} - \tilde{y}_{\mathrm{ini}}, \\
e^6 (\tilde{y}) &= \tilde{y}|_{\partial \Omega} - \tilde{y}_{\mathrm{bc}}.
\end{aligned} \tag{21}$$

Let $\lambda \equiv (p_1, p_2, p_3, q_1, q_2, q_3) \in Z$, then the Lagrangian for the problem (12)-(18) reads

$$\begin{aligned}
L(y, \tilde{y}, u, \lambda) =\,& J(y, \tilde{y}, u) + \lambda \left(e(y, \tilde{y}, u) \right) \\
=\,& \frac{1}{2} \int_{\Omega} \left| \tilde{y}|_{t=T} - \tilde{y}_f \right|^2 \mathrm{d}x + \frac{\alpha}{2} \int_0^T \int_{\partial \Omega} |u|^2 \, \mathrm{d}S \mathrm{d}t \\
& + \int_0^T \int_{\Omega} (y_t - \Delta y - H \tilde{y}_t) \, p_1 \mathrm{d}x \mathrm{d}t + \int_{\Omega} (y|_{t=0} - y_{\mathrm{ini}}) \, p_2 \mathrm{d}x + \int_0^T \int_{\partial \Omega} (y|_{\partial \Omega} - u) \, p_3 \mathrm{d}S \mathrm{d}t \\
& + \int_0^T \int_{\Omega} \left(\gamma \xi^2 \tilde{y}_t - \xi^2 \Delta \tilde{y} - \tilde{y}(1 - \tilde{y}) \left(\tilde{y} - \frac{1}{2} \right) + \beta \xi (y - y_{\mathrm{mt}}) \right) q_1 \mathrm{d}x \mathrm{d}t \\
& + \int_{\Omega} (\tilde{y}|_{t=0} - \tilde{y}_{\mathrm{ini}}) \, q_2 \mathrm{d}x + \int_0^T \int_{\partial \Omega} (\tilde{y}|_{\partial \Omega} - \tilde{y}_{\mathrm{bc}}) \, q_3 \mathrm{d}S \mathrm{d}t.
\end{aligned} \tag{22}$$

Consider $(v, \hat{v}) \in Y$, then

$$
L_{(y,\tilde{y})}\left(y,\tilde{y},u,\lambda\right)\left[(v,\hat{v})\right] = \int_{\Omega} \left(\tilde{y}|_{t=T} - \tilde{y}_f\right)\hat{v}|_{t=T}\,\mathrm{d}x + \overbrace{\int_0^T \int_{\Omega} \left(v_t - \Delta v - H\hat{v}_t\right)p_1 \mathrm{d}x \mathrm{d}t}^{I.}
$$

$$
+ \int_{\Omega} v|_{t=0}\,p_2\mathrm{d}x + \int_0^T \int_{\partial\Omega} v|_{\partial\Omega}\,p_3\mathrm{d}S\mathrm{d}t
$$

$$
+ \overbrace{\int_0^T \int_{\Omega} \left(\gamma\xi^2\hat{v}_t - \xi^2\Delta\hat{v} + 3\tilde{y}^2\hat{v} - 3\tilde{y}\hat{v} + \frac{1}{2}\hat{v} + \beta\xi v\right)q_1\mathrm{d}x\mathrm{d}t}^{II.}
$$

$$
+ \int_{\Omega} \hat{v}|_{t=0}\,q_2\mathrm{d}x + \int_0^T \int_{\partial\Omega} \hat{v}|_{\partial\Omega}\,q_3\mathrm{d}S\mathrm{d}t. \tag{23}
$$

Condition (8) is satisfied if and only if

$$
L_{(y,\tilde{y})}\left(y,\tilde{y},u,\lambda\right)\left[(v,\hat{v})\right] = 0 \text{ for all } (v,\hat{v}) \in Y.
$$

To this end, we use Greens formula to offload the derivatives in expressions I. and II. Expression I. then becomes

$$
I. = -\int_0^T \int_{\Omega} (p_1)_t\,v\mathrm{d}x\mathrm{d}t + \int_{\Omega} (p_1 v)|_{t=T} - (p_1 v)|_{t=0}\,\mathrm{d}x + \int_0^T \int_{\Omega} \nabla p_1 \cdot \nabla v \mathrm{d}x\mathrm{d}t
$$

$$
- \int_0^T \int_{\partial\Omega} p_1 \nabla v \cdot \boldsymbol{n}\mathrm{d}S\mathrm{d}t + \int_0^T \int_{\Omega} H(p_1)_t\,\hat{v}\mathrm{d}x\mathrm{d}t + \int_{\Omega} -H(p_1\hat{v})|_{t=T} + H(p_1\hat{v})|_{t=0}\,\mathrm{d}x
$$

$$
= -\int_0^T \int_{\Omega} (p_1)_t\,v\mathrm{d}x\mathrm{d}t + \int_{\Omega} (p_1 v)|_{t=T} - (p_1 v)|_{t=0}\,\mathrm{d}x - \int_0^T \int_{\Omega} \Delta p_1 v\mathrm{d}x\mathrm{d}t + \int_0^T \int_{\partial\Omega} v\nabla p_1 \cdot \boldsymbol{n}\mathrm{d}S\mathrm{d}t
$$

$$
- \int_0^T \int_{\partial\Omega} p_1 \nabla v \cdot \boldsymbol{n}\mathrm{d}S\mathrm{d}t + \int_0^T \int_{\Omega} H(p_1)_t\,\hat{v}\mathrm{d}x\mathrm{d}t + \int_{\Omega} -H(p_1\hat{v})|_{t=T} + H(p_1\hat{v})|_{t=0}\,\mathrm{d}x. \tag{24}
$$

Analogously, expression II. can be rewritten as

$$
II. = -\int_0^T \int_{\Omega} \gamma\xi^2(q_1)_t\,\hat{v}\mathrm{d}x\mathrm{d}t + \int_{\Omega} \gamma\xi^2(q_1\hat{v})|_{t=T} - \gamma\xi^2(q_1\hat{v})|_{t=0}\,\mathrm{d}x
$$

$$
+ \xi^2 \left[\int_0^T \int_{\Omega} -\Delta q_1\hat{v}\mathrm{d}x\mathrm{d}t - \int_0^T \int_{\partial\Omega} q_1\nabla\hat{v}\cdot\boldsymbol{n}\mathrm{d}S\mathrm{d}t + \int_0^T \int_{\partial\Omega} \hat{v}\nabla q_1\cdot\boldsymbol{n}\mathrm{d}S\mathrm{d}t\right]
$$

$$
+ \int_0^T \int_{\Omega} \left(3\tilde{y}^2 q_1 - 3\tilde{y}q_1 + \frac{1}{2}q_1\right)\hat{v}\mathrm{d}x\mathrm{d}t + \int_0^T \int_{\Omega} \beta\xi q_1 v\mathrm{d}x\mathrm{d}t. \tag{25}
$$

Using (24), (25) along with (23) results in

$$
\begin{aligned}
L_{(y,\tilde{y})}\left(y,\tilde{y},u,\lambda\right)\left[(v,\hat{v})\right] = & \int_{\Omega}\left(\tilde{y}|_{t=T}-\tilde{y}_f-Hp_1|_{t=T}+\gamma\xi^2 q_1|_{t=T}\right)\hat{v}|_{t=T}\,\mathrm{d}x \\
& + \int_0^T\int_{\Omega}\left(-(p_1)_t-\Delta p_1+\beta\xi q_1\right)v\mathrm{d}x\mathrm{d}t+\int_{\Omega}(p_2-p_1)|_{t=0}\,v|_{t=0}\,\mathrm{d}x \\
& + \int_0^T\int_{\partial\Omega}v\left(\nabla p_1\cdot\boldsymbol{n}+p_3\right)\mathrm{d}S\mathrm{d}t-\int_0^T\int_{\partial\Omega}p_1\nabla v\cdot\boldsymbol{n}\mathrm{d}S\mathrm{d}t+\int_{\Omega}(p_1 v)|_{t=T}\,\mathrm{d}x \\
& + \int_0^T\int_{\Omega}\left(-\gamma\xi^2(q_1)_t-\xi^2\Delta q_1+H(p_1)_t+3\tilde{y}^2 q_1-3\tilde{y}q_1+\frac{1}{2}q_1\right)\hat{v}\mathrm{d}x\mathrm{d}t \\
& + \int_{\Omega}\left(Hp_1-\gamma\xi^2 q_1+q_2\right)\hat{v}|_{t=0}\,\mathrm{d}x-\int_0^T\int_{\partial\Omega}\xi^2 q_1\nabla\hat{v}\cdot\boldsymbol{n}\mathrm{d}S\mathrm{d}t \\
& + \int_0^T\int_{\partial\Omega}\left(q_3+\xi^2\nabla q_1\cdot\boldsymbol{n}\right)\hat{v}|_{\partial\Omega}\,\mathrm{d}S\mathrm{d}t. & (26)
\end{aligned}
$$

From (26), we see that by providing a p_1 that solves

$$
\begin{aligned}
(p_1)_t+\Delta p_1 &=\beta\xi q_1 & &\text{in }(0,T)\times\Omega,\\
p_1|_{\partial\Omega} &=0 & &\text{on }\partial\Omega\times[0,T],\\
p_1|_{t=T} &=0 & &\text{in }\Omega & (27)
\end{aligned}
$$

and a q_1 that solves

$$
\begin{aligned}
\gamma\xi^2(q_1)_t+\xi^2\Delta q_1 &=H(p_1)_t+3\tilde{y}^2 q_1-3\tilde{y}q_1+\frac{1}{2}q_1 & &\text{in }(0,T)\times\Omega,\\
q_1|_{\partial\Omega} &=0 & &\text{on }\partial\Omega\times[0,T],\\
q_1|_{t=T} &=\frac{1}{\gamma\xi^2}\left(\tilde{y}_f-\tilde{y}|_{t=T}\right) & &\text{in }\Omega & (28)
\end{aligned}
$$

(in the weak sense) causes (26) to reduce to

$$
L_{(y,\tilde{y})}\left(y,\tilde{y},u,\lambda\right)\left[(v,\hat{v})\right]=\int_{\Omega}(p_2-p_1)|_{t=0}\,v|_{t=0}\,\mathrm{d}x+\int_0^T\int_{\partial\Omega}v\left(\nabla p_1\cdot\boldsymbol{n}+p_3\right)\mathrm{d}S\mathrm{d}t \qquad (29)
$$

$$
+\int_{\Omega}\left(Hp_1-\gamma\xi^2 q_1+q_2\right)\hat{v}|_{t=0}\,\mathrm{d}x+\int_0^T\int_{\partial\Omega}\left(q_3+\xi^2\nabla q_1\cdot\boldsymbol{n}\right)\hat{v}|_{\partial\Omega}\,\mathrm{d}S\mathrm{d}t.
$$

$$
(30)
$$

Lastly, we set

$$
\begin{aligned}
p_2 &= p_1|_{t=0}\,, \\
p_3 &= -\nabla p_1 \cdot \boldsymbol{n}|_{\partial\Omega}\,, \\
q_2 &= \left(\gamma\xi^2 q_1 - Hp_1\right)|_{t=0}\,, \\
q_3 &= -\xi^2 \nabla q_1 \cdot \boldsymbol{n}|_{\partial\Omega}
\end{aligned}
\tag{31}
$$

so that (30) becomes the zero operator. Next, we notice that the problems (27) and (28) can be transformed using

$$
t \to T - t.
$$

We use the following notation for the transformed variables

$$
\begin{aligned}
p(t) &= p_1(T-t)\,, \\
q(t) &= q_1(T-t)\,, \\
\tilde{z}(t) &= \tilde{y}(T-t)\,.
\end{aligned}
\tag{32}
$$

This gives rise to the well posed problem

$$
\begin{aligned}
p_t &= \Delta p - \beta\xi q && \text{in } (0,T)\times\Omega, \\
p|_{\partial\Omega} &= 0 && \text{on } \partial\Omega\times[0,T], \\
p|_{t=0} &= 0 && \text{in } \Omega,
\end{aligned}
\tag{33}
$$

$$
\begin{aligned}
\gamma\xi^2 q_t &= \xi^2\Delta q + Hp_t - 3\tilde{z}^2 q + 3\tilde{z}q - \frac{1}{2}q && \text{in } (0,T)\times\Omega, \\
q|_{\partial\Omega} &= 0 && \text{on } \partial\Omega\times[0,T], \\
q|_{t=0} &= \frac{1}{\gamma\xi^2}\left(\tilde{y}_f - \tilde{y}|_{t=T}\right) && \text{in } \Omega,
\end{aligned}
\tag{34}
$$

where the equations for p,q resemble the heat equation (13) and the Allen-Cahn equation (16), respectively, but with rather different reaction terms on the right hand side. After the system (33)-(34) is solved and the additional adjoint variables are set according to (31), the formula (7) can be used to compute the gradient of $\hat{J}$. Notice, that the first term in (7) is zero since (8) is satisfied. Let $s \in U$ be a functional variation, then the formal Fréchet derivative at point $u \in U$ in direction s reads

$$
\hat{J}'(u)[s] = \alpha \int_0^T \int_{\partial\Omega} us\,\mathrm{d}S\mathrm{d}t - \int_0^T \int_{\partial\Omega} p_3 s\,\mathrm{d}S\mathrm{d}t.
\tag{35}
$$

The numerical experiments performed in Sections 5.1.1, 5.1.3 and 5.2.1 show that using the linear reaction term (19) produces nonphysical results due to the condition (20) being violated by the optimal control. To rectify this, we additionally consider using an alternative reaction term [28]

$$
f_0(y,\tilde{y};\xi) = 2\tilde{y}(1-\tilde{y})\left(\tilde{y} - \frac{1}{2} + \xi\beta\frac{1}{2}\Sigma(\tilde{y};\varepsilon_0,\varepsilon_1)(y_{\mathrm{mt}} - y)\right),
\tag{36}
$$

where $\Sigma\left(p;\varepsilon_0,\varepsilon_1\right)$ is a differentiable sigmoid function (a limiter) in the form

$$\Sigma\left(\tilde{y};\varepsilon_0,\varepsilon_1\right) = \begin{cases} 0 & \tilde{y} \le \varepsilon_0, \\ 1 & \tilde{y} \ge \varepsilon_1, \\ \frac{3(\tilde{y}-\varepsilon_0)^2}{(\varepsilon_1-\varepsilon_0)^2} - \frac{2(\tilde{y}-\varepsilon_0)^3}{(\varepsilon_1-\varepsilon_0)^3} & \tilde{y} \in (\varepsilon_0,\varepsilon_1). \end{cases} \tag{37}$$

Since (36) does not lose its physical interpretation for any value of undercooling [28], replacing (19) with (36) allows us to obtain meaningful controls for a broader range of experiments (see Section 5.2).

The derivation of the corresponding adjoint equations is analogous to the steps leading from (21) to (33) and (34). The resulting problem reads

$$
\begin{aligned}
p_t &= \Delta p - \beta \xi q \left(\tilde{z}\Sigma\left(\tilde{z};\varepsilon_0,\varepsilon_1\right) - \tilde{z}^2\Sigma\left(\tilde{z};\varepsilon_0,\varepsilon_1\right)\right) \text{ in } (0,T)\times\Omega, & \text{in } (0,T)\times\Omega, \\
p|_{\partial\Omega} &= 0, & \text{on } \partial\Omega\times[0,T], \\
p|_{t=0} &= 0, & \text{in } \Omega, \quad (38)
\end{aligned}
$$

$$
\begin{aligned}
\gamma\xi^2 q_t &= \xi^2\Delta q + H p_t - 3\tilde{z}^2 q + 3\tilde{z}q - \frac{1}{2}q - qh\left(\tilde{z},z\right) & \text{in } (0,T)\times\Omega, \\
q|_{\partial\Omega} &= 0 & \text{on } \partial\Omega\times[0,T], \\
q|_{t=0} &= \frac{1}{\gamma\xi^2}\left(\tilde{y}_f - \tilde{y}|_{t=T}\right) & \text{in } \Omega, \quad (39)
\end{aligned}
$$

where $z(t) = y(T-t)$ and

$$h\left(\tilde{z},z\right) = \beta\left(z - y_{\mathrm{mt}}\right)\left(\Sigma\left(\tilde{z};\varepsilon_0,\varepsilon_1\right) + \tilde{z}\Sigma'\left(\tilde{z};\varepsilon_0,\varepsilon_1\right) - 2\tilde{z}\Sigma\left(\tilde{z};\varepsilon_0,\varepsilon_1\right) - \tilde{z}^2\Sigma'\left(\tilde{z};\varepsilon_0,\varepsilon_1\right)\right).$$

The gradient computation (35) and the relationships (31), (32) still hold in this case. Consequently, the gradient evaluation for the phase field system with (36) as the reaction term is straightforward.

4 General Numerical Framework

This section introduces the numerical method that is used to solve the optimization problem (12)-(18). Following the First-Optimize-Then-Discretize Paradigm [19, 26], optimality conditions are provided along with an overview of their numerical treatment (Section 4.1). This results in several sub-problems, addressed thoroughly in the section that follows (Section 4.2).

4.1 Numerical Treatment using the First-Optimize-Then-Discretize Paradigm

When following the classical first-optimize-then-discretize approach [19, 26] formally, optimality conditions are derived and then discretized to give a well formulated finite dimensional minimization problem that can then be solved numerically. Let $(\bar{y},\bar{u})$ be a solution of the problem (2)-(3) and λ_0 the solution to the corresponding adjoint problem (8). Then the optimality conditions read

$$L_\lambda\left(\bar{y},\bar{u},\lambda_0\right)=e\left(\bar{y},\bar{u}\right)=0, \tag{40}$$

$$L_y\left(\bar{y},\bar{u},\lambda_0\right)=e_y\left(\bar{y},\bar{u}\right)^*\lambda_0+J_y\left(\bar{y},\bar{u}\right)=0, \tag{41}$$

$$L_u\left(\bar{y},\bar{u},\lambda_0\right)s=J_u\left(\bar{y},\bar{u}\right)s+\left\langle\lambda_0,e_u\left(\bar{y},\bar{u}\right)s\right\rangle_Z\geq0\quad\forall s\in U. \tag{42}$$

The conditions (40)-(42) state that $(\bar{y},\bar{u},\lambda_0)$ satisfy the state equation (1), the adjoint problem (8), and the necessary condition for a local minimum. The equations (40) and (41) are then discretized using a suitable numerical method. For example, if (40) and (41) represent a system of PDE's with the requisite (initial and/or boundary) conditions, the finite difference method (FDM) or the finite element method (FEM) can be applied. Condition (42) is approximated numerically by plugging in the suitably interpolated numerical solutions of (40), (41).

For the discussion of the individual steps of the procedure, note that particular form of the primary problem (40) is given by (13)-(18) and the adjoint problem (41) takes the form of (33)-(34) or (38)-(39). Both these problems can be solved numerically by the FDM, using a fixed time step Δt and a rectangular spatial mesh. Let the numerical solution of the state equation y_h, the control u_h, and the adjoint variable λ_h all be mesh functions, i.e. functions only defined on a discrete (sub)set of mesh points. We denote the spaces of these functions as Y_h, U_h, and Z_h, respectively. The subscript h merely indicates that the dimension of these spaces is finite. The actual dimensions of these spaces depend on the number of mesh points and time levels used. The algorithm to solve the discrete counterpart of (40)-(42) then reads:

1. Start with an initial guess $u_h := u_{h,0} \in U_h$.
2. Use the FDM numerical solver to compute the solution of the primary problem $y_h\left(u_h\right) \in Y_h$.
3. Using the solution of the primary problem $y_h\left(u_h\right)$, run the FDM adjoint problem solver to compute $\lambda_h\left(y_h\left(u_h\right)\right) \in Z_h$.
4. Compute all components of $\nabla\hat{J}_h$, i.e. the partial derivatives of the discrete analogue of $\hat{J}$ with respect to all the basis vectors of U_h, using a discretization of the left hand side of (42) with λ_h obtained in the previous step.
5. Perform one step of gradient descent by updating u_h as $u_h := u_h - \varepsilon\nabla\hat{J}_h$ where $\varepsilon > 0$ is a given step size.
6. Go to step 2 unless a suitable stopping criterion is satisfied.

Some of the possible stopping criteria include exceeding a given maximum number of iterations or $\left|\nabla\hat{J}_h\right|$ falling below a predetermined threshold [19].

4.2 Details of the Numerical Method

In this section, the detailed numerical treatment of each of the problems outlined in Section 3 is laid out.

As the numerical results presented later in Section 5 are limited to one and two spatial dimensions, it is enough to follow the notation for the two-dimensional case. The one-dimensional case then arises as a straightforward simplification.

4.2.1 Finite Difference Scheme

Let $\Omega = (0,L_{x_1}) \times (0,L_{x_2}) \subset \mathbb{R}^2$, $x = (x_1,x_2)$, and $T > 0$. Both the adjoint and the primary problems are solved using the finite difference method on a uniform mesh. The time step

and the spatial mesh resolution are

$$\Delta t = \frac{T}{N_t - 1}, \ \Delta x_1 = \frac{L_{x_1}}{N_{x_1} - 1}, \ \Delta x_2 = \frac{L_{x_2}}{N_{x_2} - 1},$$

where N_t denotes the number of time layers and N_{x_1}, N_{x_2} the number of mesh points in the x_1 and x_2 directions, respectively. The explicit Euler scheme is employed. Let f be a real-valued function defined on $(0,T) \times \Omega$ and f_h be its approximation by the respective mesh function. Then we replace the time derivative of f by

$$f_t(k\Delta t, i\Delta x_1, j\Delta x_2) \approx f_{h,t}(k\Delta t, i\Delta x_1, j\Delta x_2) \equiv \frac{f_h((k+1)\Delta t, i\Delta x_1, j\Delta x_2) - f_h(k\Delta t, i\Delta x_1, j\Delta x_2)}{\Delta t}.$$
$$(43)$$

For the discretization of the Laplacian of f, the central difference quotient

$$\Delta f(k\Delta t, i\Delta x_1, j\Delta x_2) \approx \Delta_h f_h(k\Delta t, i\Delta x_1, j\Delta x_2) \equiv \quad (44)$$

$$\frac{f_h(k\Delta t, (i+1)\Delta x_1, j\Delta x_2) - 2f_h(k\Delta t, i\Delta x_1, j\Delta x_2) + f_h(k\Delta t, (i-1)\Delta x_1, j\Delta x_2)}{(\Delta x_1)^2} \quad (45)$$

$$+ \frac{f_h(k\Delta t, i\Delta x_1, (j+1)\Delta x_2) - 2f_h(k\Delta t, i\Delta x_1, j\Delta x_2) + f_h(k\Delta t, i\Delta x_1, (j-1)\Delta x_2)}{(\Delta x_2)^2} \quad (46)$$

is used.

4.2.2 Numerical Integration

The integral in (35) is evaluated using a piece-wise constant interpolation as follows. Let Π be a subset of the Cartesian rectangular mesh representing the boundary ($[0,T] \times \partial\Omega$) and let $f_h : \Pi \to \mathbb{R}$, $s_h : \Pi \to \mathbb{R}$ be mesh functions. To improve readability, the subscript h is dropped for both f_h and s_h in this section.

Let S_Π be an interpolation operator that transforms a mesh function on Π to a piecewise (a.e.) constant function on $[0,T] \times \partial\Omega$. More precisely, the definition of S_Π on the bottom edge ($x_2 = 0$) of a rectangular 2D domain reads

$$S_\Pi f(t, x_1, 0) = f_{k,i,0} \text{ for } (t, x_1, 0) \in M_{k,i,0},$$

where

$$M_{k,i,0} = \left(\max\left(0, (k-1)\Delta t + \frac{\Delta t}{2}\right), \min\left(T, k\Delta t + \frac{\Delta t}{2}\right) \right)$$
$$\times \left(\max\left(0, (i-1)\Delta x_1 + \frac{\Delta x}{2}\right), \min\left(L_{x_1}, i\Delta x_1 + \frac{\Delta x_1}{2}\right) \right) \times \{0\},$$

k denotes the time level and i represents the mesh point position along the x_1 axis. Intuitively, the set $M_{k,i,0}$ can be viewed as a rectangle in $(0,T) \times \partial\Omega$ centered in $(k\Delta t, i\Delta x_1, 0)$ except for $k = 0, N_t, i = 0, N_x$, where there is a "cut-off" at the boundary. The operator S_Π is

defined analogously for the other edges. Since the numerical scheme described by (43)-(44) does not require the points in the corners of the spatial domain Ω, they are left out in the approximation of (35), giving rise to

$$
\int_0^T \int_{\partial\Omega} (S_\Pi f)(S_\Pi s)\, \mathrm{d}S \mathrm{d}t \approx \sum_{k=0}^{N_t-1} \sum_{i=1}^{N_{x_1}-1} \left[f_{k,i,0} s_{k,i,0} + f_{k,i,N_{x_2}} s_{k,i,N_{x_2}} \right] \Delta t \Delta x_1
$$
$$
+ \sum_{k=0}^{N_t-1} \sum_{j=1}^{N_{x_2}-1} \left[f_{k,0,j} s_{k,0,j} + f_{k,N_{x_1},j} s_{k,N_{x_1},j} \right] \Delta t \Delta x_2, \qquad (47)
$$

where j represents the mesh point position along the x_2 axis and $\alpha = 0$ is chosen for simplicity. Notice that omitting the corners of the spatial domain does not affect the convergence of (47) as $N_t, N_{x_1}, N_{x_2} \to +\infty$.

In particular, (47) will be used along with a finite difference approximation $p_{3,h}$ of p_3 in (31) to get the computation rule for the k, i, j-th component of the gradient as

$$
\int_0^T \int_{\partial\Omega} (S_\Pi p_{3,h})(S_\Pi e_{k,i,j})\, \mathrm{d}S \mathrm{d}t = \begin{cases} (p_{3,h})_{k,i,j} \Delta t \Delta x_1 & \text{if } j = \{1, N_{x_2}-1\}, \\ (p_{3,h})_{k,i,j} \Delta t \Delta x_2 & \text{if } i = \{1, N_{x_1}-1\}, \end{cases} \qquad (48)
$$

where $e_{k,i,j}$ is the characteristic function of $M_{k,i,j}$. Since p (see (33)) is subject to the homogeneous Dirichlet boundary condition, the approximation $p_{3,h}$ in the gradient computation (48) reduces to the interior values of p_1 (see (32), (31)) adjacent to the boundary $\partial\Omega$.

5 Numerical Results

Utilizing the adjoint formulations derived in Section 3 and the corresponding numerical treatments detailed in Section 4, the problem (12)-(18) is solved numerically. In Section 5.1, simulations in one spatial dimension using the linear reaction term (19) are performed and the effects of regularization, changes in final time and different initial guesses are discussed. Several scenarios where the bound (20) is not violated are shown. Some of the experiments, however, show that the optimal control violates the bound (20) in order to achieve the desired crystal shape (see some of the experiments in Section 5.1 and the experiment of Section 5.1.3). When this is the case, we call a simulation or associated optimal control *non-realistic*.

As expected, this inadequacy can be observed in experiments with two spatial dimensions as well (see Section 5.2). In Section 5.2.1, an experiment that directly compares the behaviors obtained using the linear reaction term (19) and the alternative reaction term (36) is described. The last experiment of the section shows how the reaction term (36) can be used to find a realistic optimal control that separates a crystal into two.

Before discussing each of the simulations in detail, some terminology and notes will be presented. When commenting on experiments, we recall the definitions (9)-(11) and the related terminology introduced in Section 3, using the terms "crystal" and "solid subdomain" interchangeably to refer to $\Omega_s(t)$. It is well known [7, 8, 28] that inside of $\Omega_s(t)$ and $\Omega_l(t)$, the value of the phase field $\tilde{y}$ is very close to 1 and 0, respectively, except for a thin transition layer between the phases near $\Gamma(t)$. For both the models considered, this transition layer (diffuse interface) has a characteristic profile with a thickness proportional

Table 1 Parameter settings for the phase field simulations in Section 5.1.

Param.	Value	Physical Meaning
γ	1	coefficient of attachment kinetics
β	2	dimensionless representation of supercooling
ξ	0.005	interface thickness scaling
y_{mt}	0.5	melting temperature
H	1	latent heat
L_x	1	spatial dimension in the x direction

to ξ. Specifically, in the one-dimensional case, let $x_0(t)$ denote the position of the phase interface (i.e. $\{x_0(t)\} = \Gamma(t)$) and $\Omega_s(t) = [0, x_0(t))$, $\Omega_l(t) = (x_0(t), 1]$. Then

$$\tilde{y}(t,x) = \frac{1}{2}\left[1 - \tanh\left(\frac{x - x_0(t)}{2\xi}\right)\right] + o(\xi). \tag{49}$$

This explanation can be extended to multiple dimensions, then the profile (49) is maintained in the direction normal to the interface [6, 28].

Denote the numerical approximation of y as y_h, the numerical approximation of $\tilde{y}$ as $\tilde{y}_h$ and let $P_h : Y \to Y_h$ be the projection operator onto the mesh.

5.1 Dirichlet Boundary Condition Control for the Phase Field Problem in 1D

All the experiments in this section are performed in one spatial dimension. Let all the physical parameters be set according to the values in Table 1. These settings do not necessarily correspond to any real material, they do however serve to illustrate the capabilities and deficiencies of the optimization problem (12)-(18) with the linear reaction term (19). Additionally, the influence of regularization α, changes in final time T and initial guess for the control are discussed in this section also.

5.1.1 Controlling the Extent of Crystal Growth

We attempt to find a control that will produce a crystal $\Omega_{s,f}$ of prescribed length inside of the spatial domain Ω at the fixed final time $T > 0$. We set the phase field boundary condition to

$$\begin{aligned}
\tilde{y}_{bc}(t,0) &= 1 & \forall t \in [0,T), \\
\tilde{y}_{bc}(t,1) &= 0 & \forall t \in [0,T),
\end{aligned} \tag{50}$$

which creates a nucleation site at $x = 0$. The initial conditions $\tilde{y}_{ini}, y_{ini}$ and the target profile $\tilde{y}_f$ are depicted in Figure 1. In this case, $\tilde{y}_f$ is merely the characteristic function of the target crystal shape $\Omega_{s,f}$. Alternatively, $\tilde{y}_f$ could be chosen as a continuous function with the characteristic shape across the interface (49), as demonstrated further in Sections 5.1.2 and 5.1.3. The initial guess for the control is

$$\begin{aligned}
u_0(t,0) &= 0 & \forall t \in [0,T), \\
u_0(t,1) &= 1 & \forall t \in [0,T).
\end{aligned} \tag{51}$$
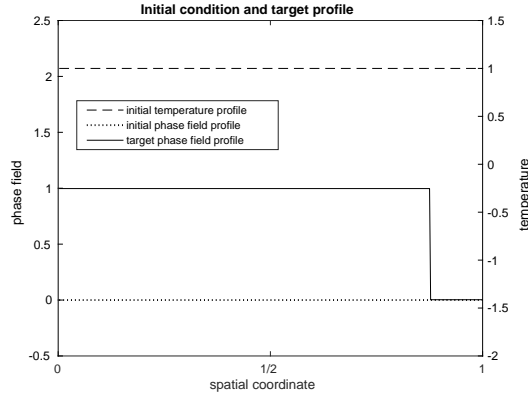
Fig. 1 The initial temperature and phase field spatial profiles $\bar{y}_{\mathrm{ini}}, y_{\mathrm{ini}}$ along with the target profile $\bar{y}_f$ for experiments 1, 2, 3. The values of the boundary condition $\bar{y}_{\mathrm{bc}}$ are given by (50).

Table 2 Settings for experiments 1, 2, 3 and the respective values of the difference (error) from the prescribed profile.

	Simulation number		
Parameter	1	2	3
number of time steps N_t	$4 \cdot 10^5$	$4 \cdot 10^5$	$4 \cdot 10^5$
number of grid points N_x	400	400	400
initial control given by	(51)	(51)	(51)
final time T	0.1	0.05	0.05
regularization parameter α	0	0	$5 \cdot 10^{-11}$
gradient descent step size ε	$3 \cdot 10^{15}$	$2 \cdot 10^{16}$	$2 \cdot 10^{16}$
number of iterations	100	100	100
$\left\| \bar{y}_h - P_h \bar{y}_f \right\|_2$ at $t = T$	1.117846	1.276584	13.64326

In this setting, three numerical experiments are presented. The parameters including the spatial mesh resolution, the number of time steps as well as the difference of the final solution from the prescribed phase field profile are summarized in Table 2.

For each of the experiments, the resulting temperature and phase field spatial profiles at final time T are depicted in Figure 2. Figure 3 shows the respective temporal control profiles of the Dirichlet boundary condition.

In experiment 1, the optimized control leads to a good agreement of the solution with the target profile at the final time $T = 0.1$. The values of u_h stay within the limits given by (20) and thus the solution is realistic. This experiment was also repeated several time with different nonzero values of the regularization parameter α. Up to the values $\alpha \approx 10^{-7}$, negligible impact of the regularization was observed. In experiment 2, the final time is halved, i.e. $T = 0.05$. The target profile was still obtained at the cost of violating the bound (20). Experiment 3 differs from experiment 2 by setting the regularization parameter to $\alpha = 5 \cdot 10^{-11}$ (i.e. $\alpha \ll 10^{-7}$, cf. Experiment 1). This was sufficient to keep the simulation realistic but the target profile was not obtained. Such a situation can be interpreted as the time T being too short for the target profile to be reached. This is true only in the context of the linear model, where f_0 is defined by (19). The use of a more advanced model, that is not limited in this way is discussed in Sections 5.2.1 and 5.2.2.
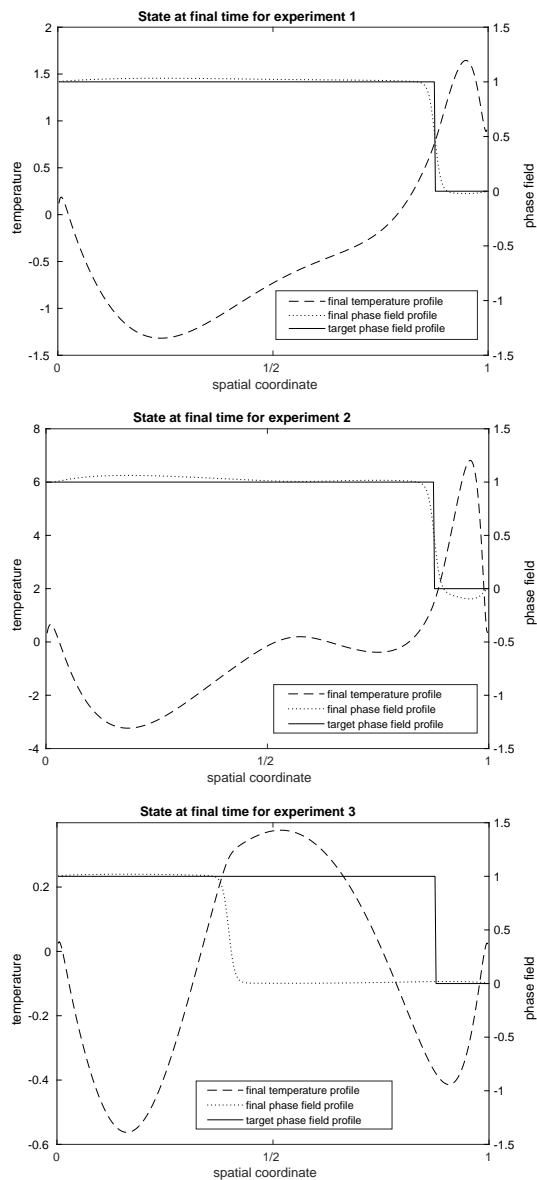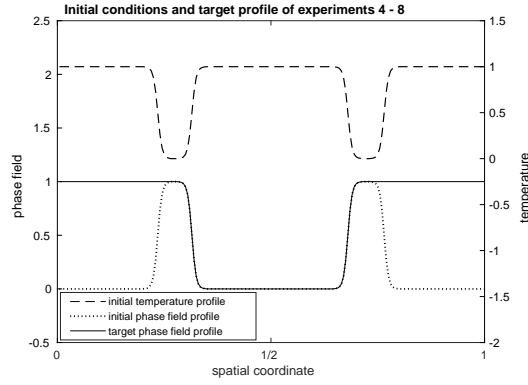
Fig. 2 Final temperature and phase field spatial profiles of experiments 1, 2, 3. We observe that $\tilde{y}_h$ reaches the target $P_h\tilde{y}_f$ in experiments 1 and 2. In experiment 3, the interface of $\tilde{y}_h$ does not reach its target $P_h\tilde{y}_f$ because sufficient regularization is added to prevent non-realistic behavior.

5.1.2 Keeping Crystal Separation

In this series of experiments, we attempt to keep two symmetrically placed crystals in the interior of the domain separated from each other, while letting them grow toward the boundaries. The target profile $\tilde{y}_f$ and initial conditions y_{ini}, $\tilde{y}_{\text{ini}}$ are depicted in Figure 4. In
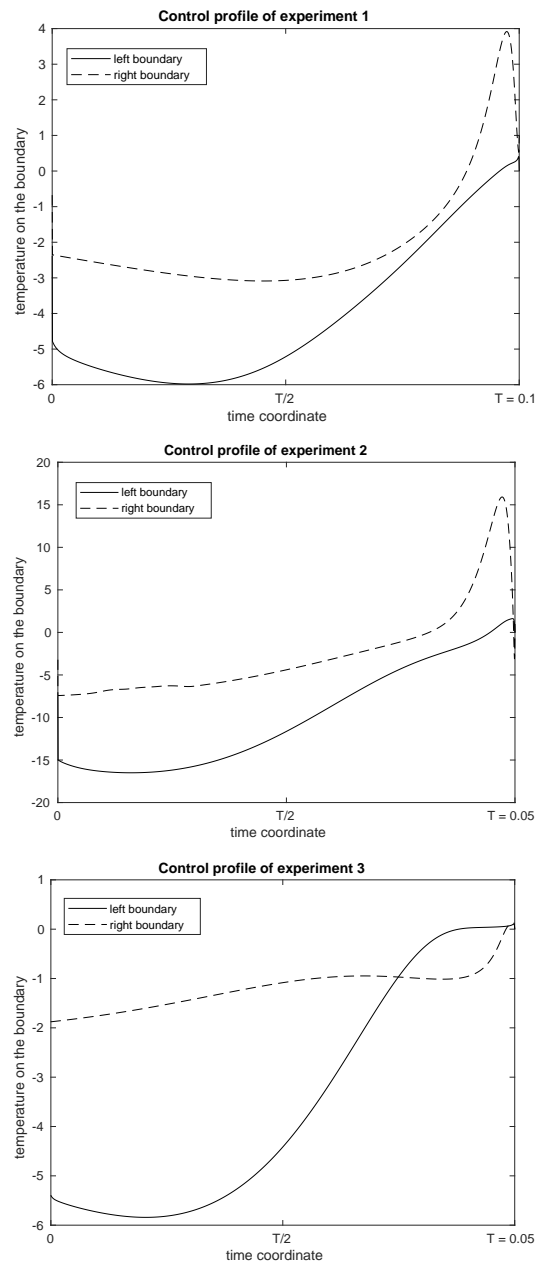
Fig. 3 Optimized temporal control profiles of experiments 1, 2, 3. In experiment 2, the values of the temperature violate the bound (20) due to the short final time T. The regularization applied in experiment 3 fixes this issue at the cost of not attaining the target profile (see Figure 2).

Fig. 4 The initial temperature and phase field profiles $\tilde{y}_{\mathrm{ini}}, y_{\mathrm{ini}}$ along with the target profile $\tilde{y}_f$ for experiments 4 through 8. The values of the boundary condition $\tilde{y}_{\mathrm{bc}}$ are given by (52).

Table 3 The settings for experiments 4 through 8 and the respective values of the difference (error) from the prescribed profile.

	Simulation Number				
Parameter	4	5	6	7	8
number of time steps N_t	10^5	10^5	10^5	10^5	10^5
number of grid points N_x	200	200	200	200	200
initial control given by	(51)	(51)	(51)	(51)	(53)
T (final time)	0.05	0.4	0.4	0.4	0.4
regularization parameter α	0	0	$5 \cdot 10^{-10}$	10^{-9}	0
gradient descent step size ε	$2 \cdot 10^{14}$	$3 \cdot 10^{13}$	10^{13}	10^{13}	$3 \cdot 10^{14}$
number of iterations	150	100	100	125	100
$\left\| \tilde{y}_h - P_h \tilde{y}_f \right\|_2$	0.3359370	0.3392653	0.4725518	0.8469198	0.3293709

contrast to Section 5.1.1, $\tilde{y}_f$ is a continuous function with a characteristic shape across the interface (49). The boundary condition for the phase field reads

$$\tilde{y}_{\mathrm{bc}}(t,x) = 1 \qquad \forall x \in \{0,1\}, \ \forall t \in [0,T]. \tag{52}$$

First, we use the non-symmetric initial control guess (51) to observe its effects on the obtained temporal profile of u_h and overall quality of minimization expressed by the error $\left\| \tilde{y}_h - P_h \tilde{y}_f \right\|_2$. Then we add regularization and use the symmetric initial guess

$$u_0(x,t) = 0 \qquad \forall x \in \{0,1\}, \ \forall t \in [0,T]. \tag{53}$$

and compare the results.

The settings of these experiments can be found in Table 3. First of all, let us emphasize that all the experiments discussed below lead to a rather accurate reproduction of the target profile. This is obvious from the values of the error $\left\| \tilde{y}_h - P_h \tilde{y}_f \right\|_2$ listed in Table 3 as well as from Figure 5 where the best and the worst final profiles are shown. Also, all the experiments in this section remain realistic since y is kept within the admissible bounds (20).

Let us now focus on the differences in the obtained temporal control profiles u_h between the individual experiments (see Figure 6).
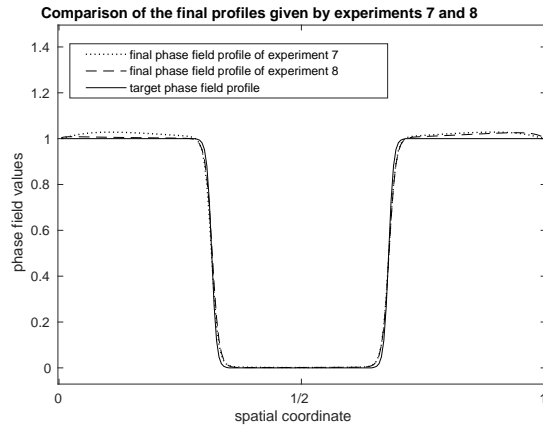
Fig. 5 Comparison of the best and the worst (in terms of the error $\left\| \tilde{y}_h - P_h \tilde{y}_f \right\|_2$) phase field profile estimations for experiments 4 through 8.

- Experiments 4 and 5 demonstrate how the choice of very different final times T ($T = 0.05$ and $T = 0.4$) affects the control u_h. When the control is given more time (experiment 5, $T = 0.4$), its action is delayed to the final part of the interval $(0, T)$. Nevertheless, the range of u_h is similar in both cases.
- Experiments 5, 6, and 7 show the effects of regularization α of different amplitudes with the fixed final time $T = 0.4$. As expected, increasing α significantly reduces the range of the control u_h. However, this does not affect the overall minimization quality substantially. This is because the action of the control is distributed over a longer time period.
- Experiment 5 and 8 show the effect of the initial guess u_0. It is not surprising that in experiment 8, a spatially symmetric problem with a symmetric initial guess (53) result in (almost) identical left and right temporal control profiles $u_h(\cdot, 0)$ and $u_h(\cdot, 1)$. Experiment 5 differs from experiment 8 only in the non-symmetry of the initial guess (51). As a consequence, the left and right temporal control profiles are completely different.
- Experiments 5, 6, and 7 also indicate that the regularization partially symmetrizes the left and the right temporal control profiles.

### 5.1.3 Moving a Gap Between Crystals

Experiment 9 showcases how even highly non-trivial control can be obtained. Consider a situation in which two crystals occupy the whole domain except for a comparatively small gap between them. We aim to move the liquid gap to a different position in the domain. This is reflected by the settings of y_{ini}, $\tilde{y}_{\text{ini}}$ and the target profile $\tilde{y}_f$ shown in Figure 7 as well as the use of the boundary condition (52). The full setup of the experiment is summarized in Table 4. Note that during optimization, the gradient descent step size was (manually) adjusted from ε_1 to ε_2 to ensure convergence.

The target profile $\tilde{y}_f$ is achieved by a rather surprising process. First, the entire domain is solidified. Afterward, the molten region is recreated next to the right boundary. As the melting proceeds to the left, the right boundary is undercooled again to create another solid subdomain on the right. The resulting control profiles for the entire time interval are
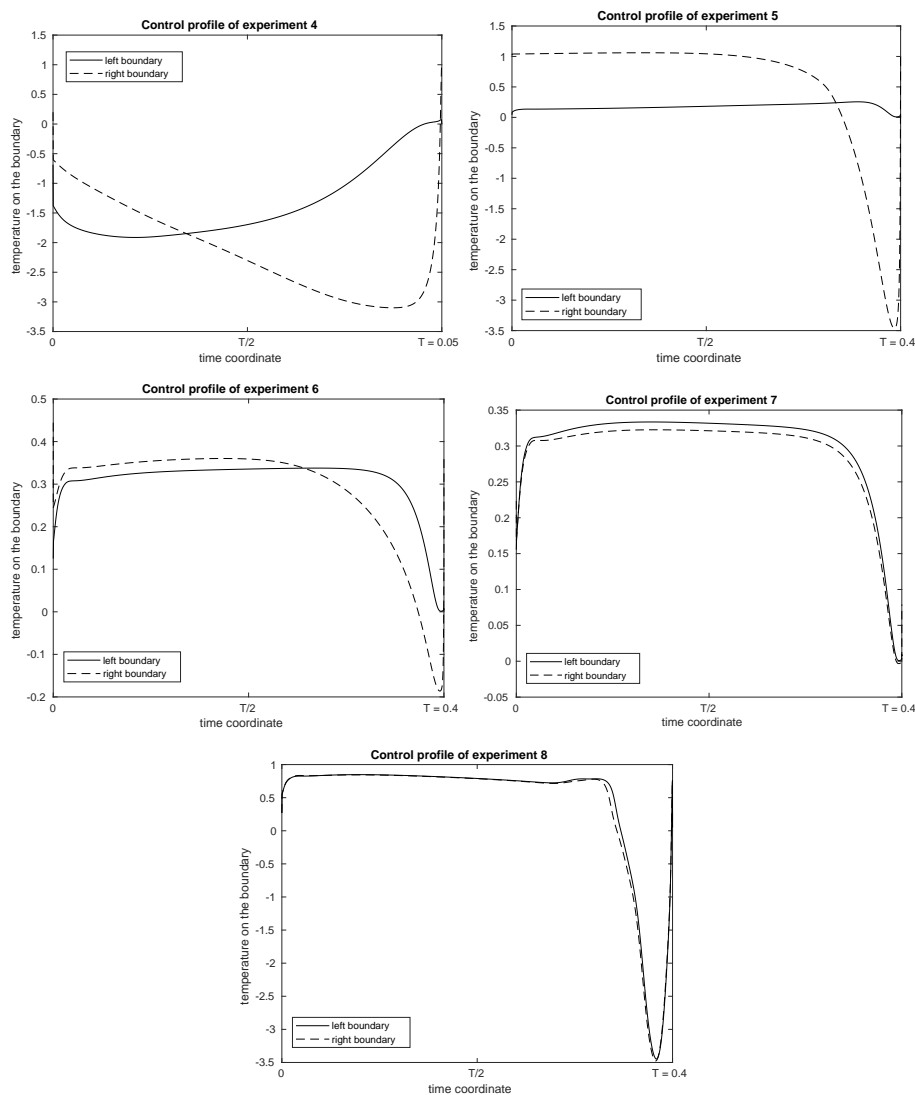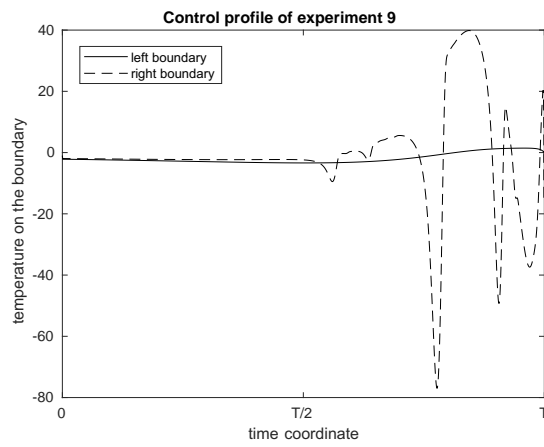
Fig. 6 Optimized temporal control profiles of experiments 4 through 8. Experiments 4 and 5 show how an optimization without regularization responds to an increase of final time T. Regularization is then added in experiments 6 and 7. The control profiles flatten and the control becomes more evenly distributed. Lastly, experiment 8 shows a different non-regularized control given by the symmetric initial condition $\tilde{u}_{\mathrm{ini}}$.

displayed in Figure 8. In addition, six snapshots of the final phase of the solution evolution are depicted in Figure 10, with the corresponding times marked in Figure 9. In terms of the condition (20), the simulation is not realistic.
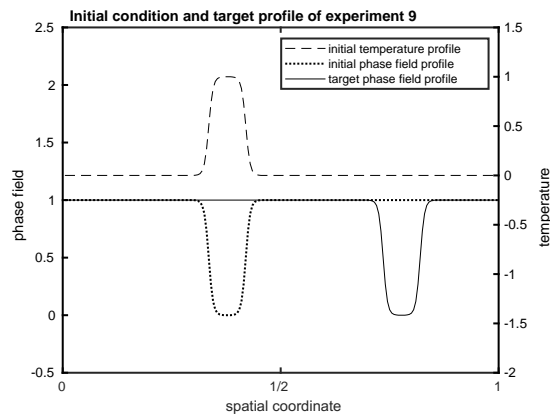
Fig. 7 The initial temperature and phase field profiles $\tilde{y}_{\mathrm{ini}}, y_{\mathrm{ini}}$ along with the target profile $\tilde{y}_f$ for experiment 9. The values of the boundary condition $\tilde{y}_{\mathrm{bc}}$ are given by (52).

Fig. 8 Temporal control profiles for experiment 9.
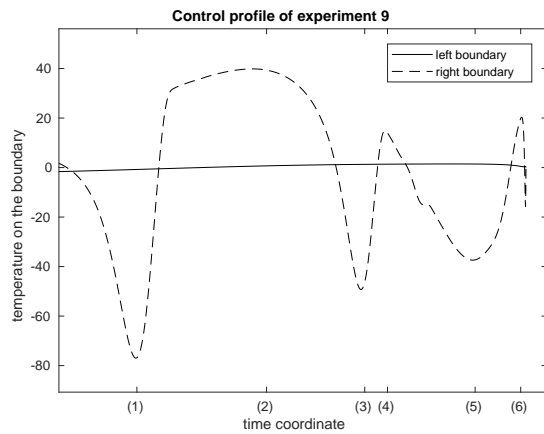
Fig. 9 A detailed look at the latter part of the temporal control profile in experiment 9.
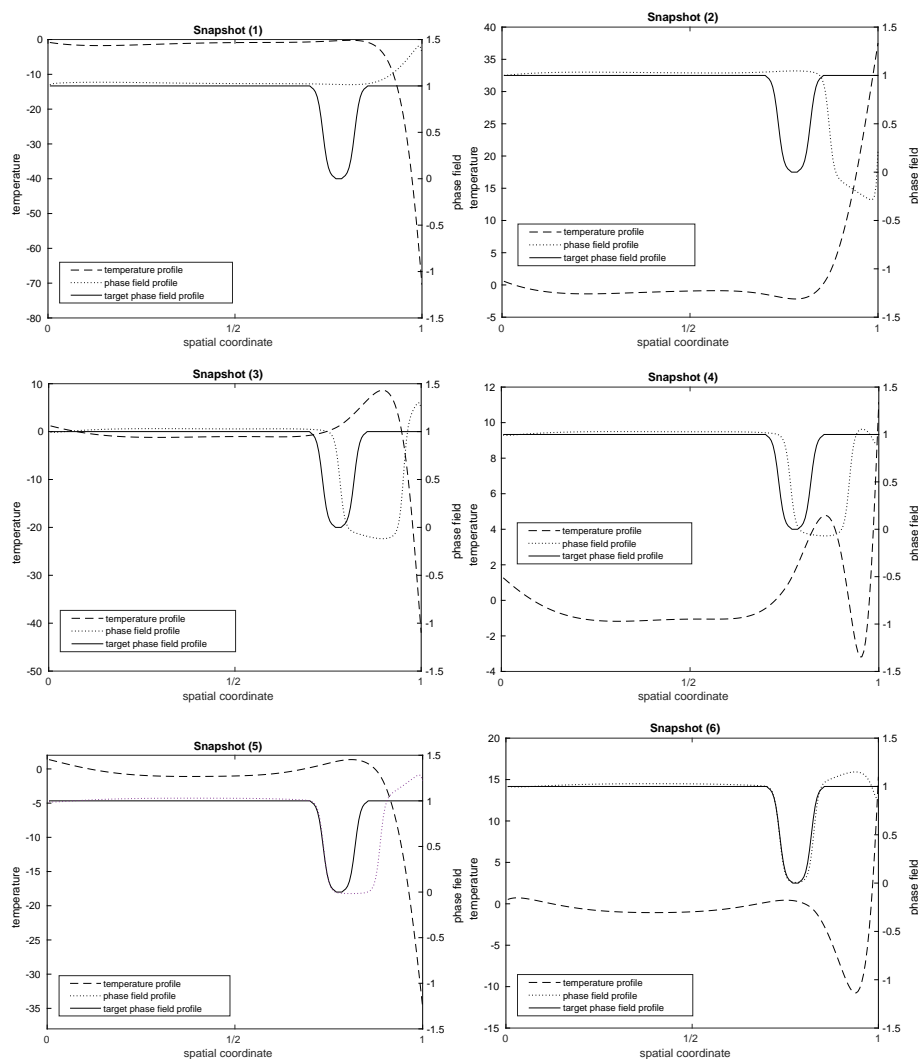
Fig. 10 The spatial profiles of the phase field and temperature at the significant times (1)–(6) marked in Figure 9.

Table 4 Settings for experiment 9 and the respective value of the difference (error) from the prescribed profile.

Parameter	Value
number of time steps N_t	10^5
number of grid points N_x	200
initial control given by	(53)
T (final time)	0.1
regularization parameter α	0
gradient descent step size ε	$\varepsilon_1 = 10^{16}$, $\varepsilon_2 = 5 \cdot 10^{15}$
number of iterations	225 with step ε_1, 25 with ε_2
$\left\lVert \tilde{y}_h - P_h \tilde{y}_f \right\rVert_2$	0.5932381

Table 5 Parameter settings for the phase field simulations in Section 5.2.

Param.	Value	Physical Meaning
γ	3.0	coefficient of attachment kinetics
β	300	dimensionless representation of supercooling
ξ	0.0101	interface thickness scaling
y_{mt}	1.0	melting temperature
H	2.0	latent heat
ε_0	0	parameter of the sigmoid function in (36)
ε_1	0.2	parameter of the sigmoid function in (36)
L_{x_1}	0.6	spatial dimension in the x_1 direction
L_{x_2}	1.0	spatial dimension in the x_2 direction

5.2 Dirichlet Boundary Condition Control for the Phase Field Problem in 2D

In the preceding Section, a bevy of examples detailed the utility and the possible shortcomings that come with using a linear reaction term (19) in (12)-(18). Among other things, the effects of regularization, changes in final time and initial guess for the control were discussed in detail. In this section, simulations in two spatial dimensions are performed. The focus will no longer be on tweaking the parameters of the simulations. Instead, we focus on the effect of using the reaction term (36) in (12)-(18) as well as showing non-trivial realistic controls that arise in some situations.

Parameters that are common to all the experiments detailed in this section are listed in Table 5.

5.2.1 Moving a Crystal from North to South with Different Reaction Terms

The aim of this set of numerical experiments is to move a crystal from one position in the domain to another, while maintaining its shape and size. Two experiments are performed. One using the linear reaction term (19) and the other uses the alternative more advanced reaction term (36).

For both of the experiments, the initial condition $\tilde{y}_{\mathrm{ini}}$ along with the target profile $\tilde{y}_f$ can be found in Figure 12. The boundary condition for the phase field $\tilde{y}$ is given by

$$\tilde{y}_{\mathrm{bc}}(t,x) = 0, \ \forall x \in \partial\Omega, \ \forall t \in [0,T]. \tag{54}$$

The initial guess for the Dirichlet control on the boundary reads

$$u_0(t,x) = 1, \ \forall x \in \partial\Omega, \ \forall t \in [0,T]. \tag{55}$$

Other data for the experiments (some of which is not common for both experiments), like the mesh resolution or the final error, can be found in Table 5 and Table 6.

The resulting temporal control profiles along with the time evolution of the level set $\Gamma(t)$ (the shape of the crystal) for both experiments can be reviewed in Figures 12, for the linear reaction term (19), and Figures 13 for the alternative term (36). Comparing the aforementioned figures shows that the two controls obtained are qualitatively and quantitatively different.

This is unsurprising, since the state equation (12)-(18) with (19) allows for spontaneous nucleation when the bound (20) is violated [28]. It has been shown that the term (36) does not suffer from such a deficiency [28] and the obtained control reflects this. As a result, only the control depicted in Figure 13 can be interpreted as solidification.
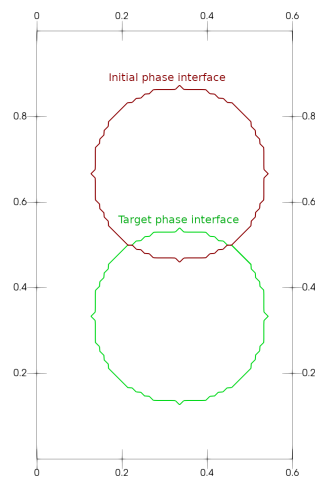
Fig. 11 Initial and target phase field interface Γ for the simulation in Section 5.2.1.
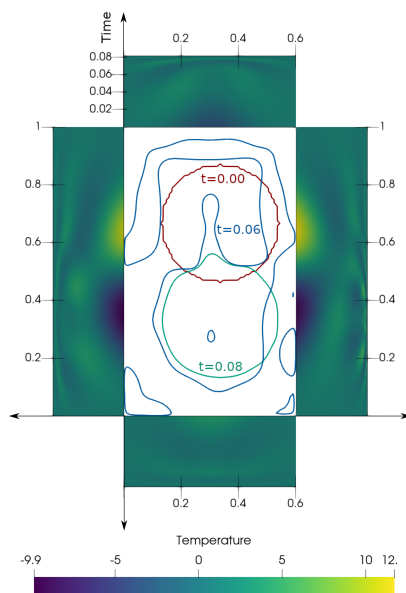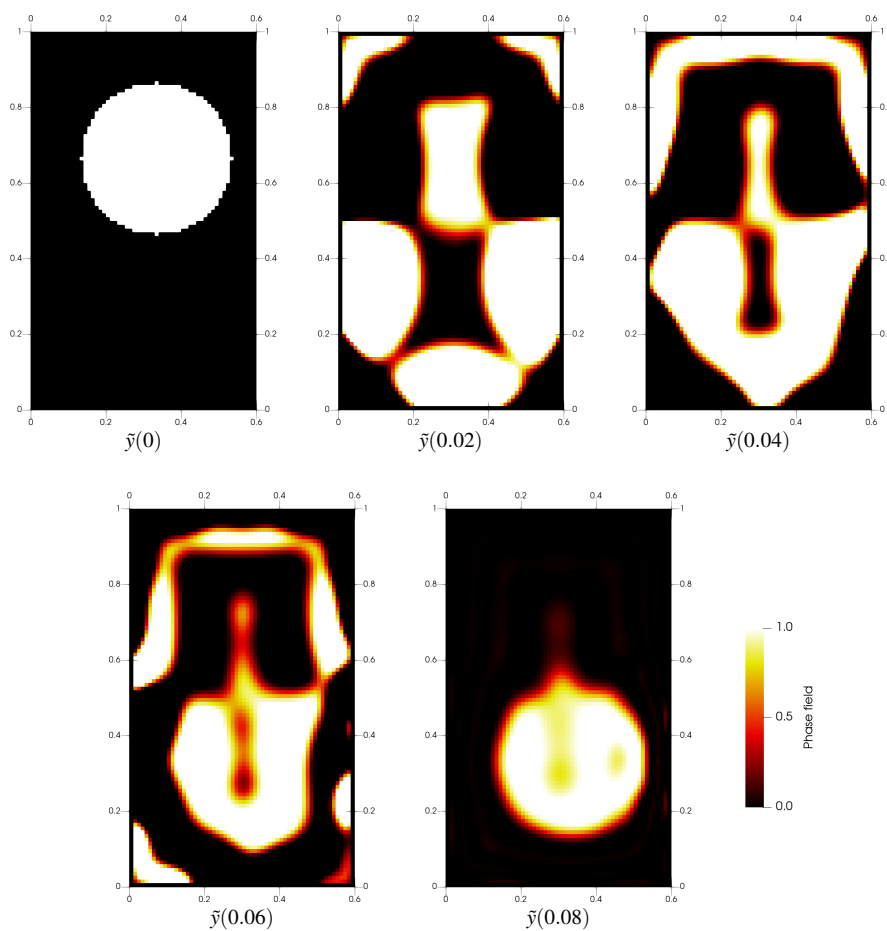

Fig. 12 Simulation with the linear reaction term (19). For details, see Section 5.2.1.
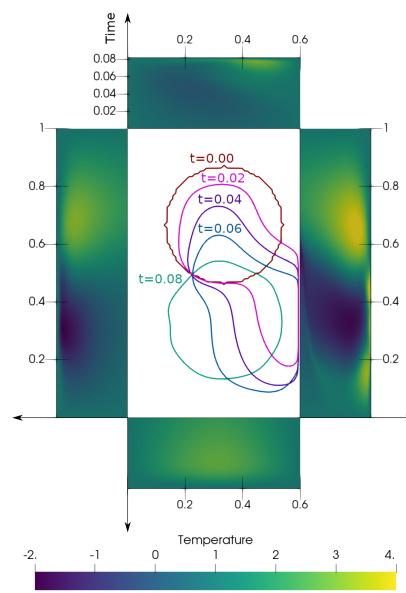
Fig. 13 Simulation with the alternative reaction term (36). For details, see Section 5.2.1.

In Figure 12, highly complex shape of the interface Γ can be observed at time $t = 0.06$ and the crystal assumes its final shape very close to the final time $t = 0.08$. More snapshots of the phase field evolution are shown in Figure 14. On the other hand, in Figure 13, the crystal keeps shape close to the original in all of the shown snapshots. In this simulation, the evolution is affected by the non-symmetric initial position of the crystal, as the evolution is driven mainly by the heating and cooling of the right boundary. A preference to keep the crystal close to the right boundary, where the Dirichlet's boundary condition has the

Fig. 14 Evolution of phase field in simulation with the linear reaction term (19). For details, see Section 5.2.1.

strongest influence, can be observed. Close to the final time $t = 0.08$, the crystal separates from the domain boundary and fine adjustments in the control shape it to match the target profile $\tilde{y}_f$. Figures 15 and 16 show the correspondence between the target phase interface and the final phase interface obtained as the result of the simulation with both reaction terms and the corresponding optimal boundary control. It may be noticed that in the case of linear reaction term, the top portion of the final crystal does not have the optimal shape while in the other case the crystal is pushed to the right. This difference is caused by the different process leading to the final state.

5.2.2 Separating a Crystal with the Improved Reaction Term

The last numerical simulation aim to address the question of crystal separation. The more advanced reaction term (36) is used. Namely, considering a single rectangular crystal in the spatial domain at initial time, a control that separates this crystal into two circular ones is sought after.
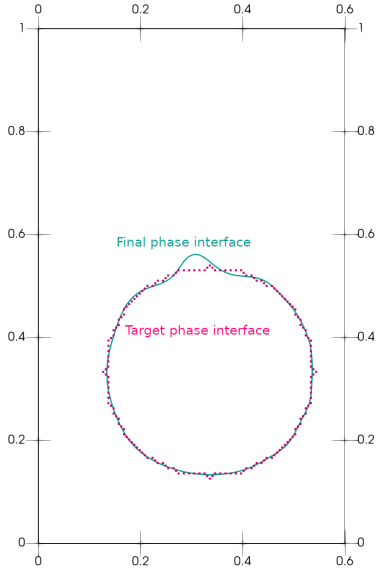
Fig. 15 Target and final phase field obtained in the simulation with the linear reaction term (19). For details, see Section 5.2.1.
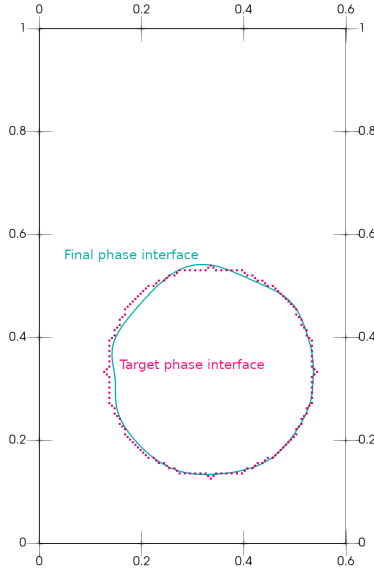
Fig. 16 Target and final phase field obtained in the simulation with the alternative reaction term (36). For details, see Section 5.2.1.

Figure 17 depicts the initial conditions $\tilde{y}_{\mathrm{ini}}$ and the target profile $\tilde{y}_f$. The boundary condition for the phase field $\tilde{y}$ is given by

$$\tilde{y}_{\mathrm{bc}}(t,x) = 0, \ \forall x \in \partial\Omega, \ \forall t \in [0,T]. \tag{56}$$

The initial guess for the Dirichlet control on the boundary reads

$$u_0(t,x) = 1, \ \forall x \in \partial\Omega, \ \forall t \in [0,T]. \tag{57}$$

Additional data for the experiment are listed in Table 6.

The time evolution of the crystal shape $\Gamma(t)$ and the temporal control profiles are combined in Figure 17.

On both sides of the domain, the optimal control exhibits an effort to heat up the center of the domain in order to separate the crystal into two. At the same time, the upper and lower parts of the domain cool down, leading to the growth of crystals at the ends of the domain. The two crystals end up being slightly deformed compared to the ones prescribed by $\tilde{y}_f$, as can be seen in Figure 19.

5.3 Performance and Implementation Details

The 1D and 2D solvers used in Section 5.2.1 and 5.2.2, respectively, were implemented in MATLAB and C++. This section intends to give the reader an idea about the performance and not to serve as a comparison of the two implementations. Therefore, the performance
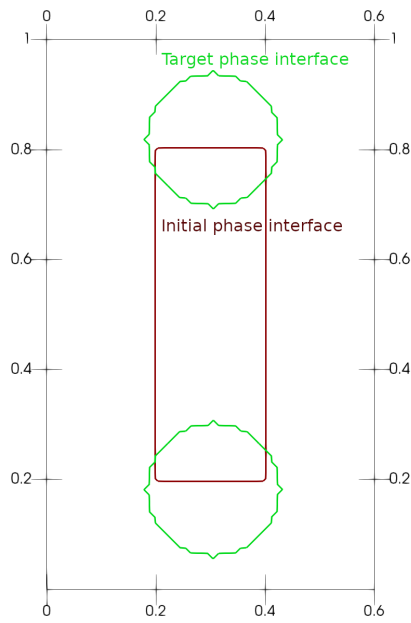
Fig. 17 The initial and target position of the phase interface Γ for the simulation in Section 5.2.2.
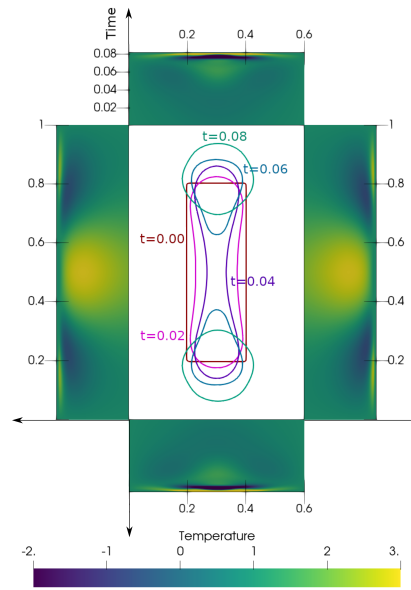
Fig. 18 The heating of the domain boundary in time and the snapshots of the phase interface $\Gamma(t)$ during the evolution and in the final time $T = 0.08$. For details on this simulation, see Section 5.2.2.
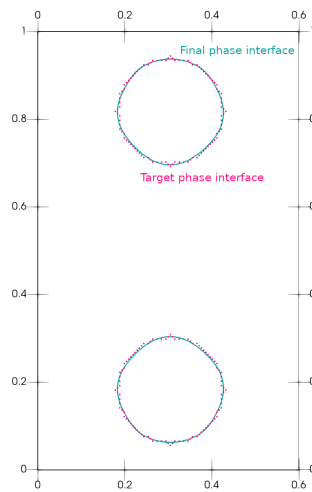
Fig. 19 Target and final phase field obtained in the simulation described in Section 5.2.2.

Table 6 Settings for the 2D experiments and the respective values of the difference (error) from the prescribed profile. The first experiment was performed with two reaction terms - linear and alternative.

Parameter	Simulation	
	Moving crystal (Section 5.2.1)	Separating crystal (Section 5.2.2)
number of time steps N_t	$8 \cdot 10^3$	$8 \cdot 10^3$
number of grid points N_x	60	60
number of grid points N_y	100	100
initial control given by	(55)	(57)
final time T	0.081	0.081
regularization parameter α	0	0
gradient descent step size ε	5.0	7.5
number of iterations	400 (linear), 5000 (alternative)	1000
$\left\| \tilde{y}_h - P_h \tilde{y}_f \right\|_2$ at $t = T$	7.66 (linear), 7.39 (alternative)	7.21

Table 7 Time to compute 100 iterations of gradient descent for different discretization resolutions. All simulations were performed on desktop with Intel B360 AORUS MB, i7-8700 CPU and 16GB RAM (Fedora 31 Linux). The values of N_t are given in multiples of 10^3.

N_x	N_y	N_t	Computational time [s]
51	51	1	37
51	101	1	78
101	101	4	585
101	101	8	1188
101	201	4	1281

analysis is only presented for the more computationally intensive 2D case. The C++ solver used in Section 5.2 was executed on a single CPU core. Simple benchmark can be reviewed in Table 7.

Conclusion

The formal adjoint problem for the numerical optimization of Dirichlet boundary condition in the phase field model was derived for two different reaction terms. The possibilities of this formulation were explored using several simulations performed in one and two spatial dimensions with the help of the finite difference method. Among other things, the influence of reaction term choice, initial control estimate and regularization are discussed. Ultimately, several experiments performed in two spatial dimensions show how even non-trivial control that may be interpreted as solidification can be obtained using this method.

Using the adjoint formulation makes it possible to achieve impressive performance figures with limited hardware and a rudimentary numerical method. This gives a positive future outlook for the application of Dirichlet boundary control optimization for crystal morphology estimation and solidification control in three dimensions.

Data availability

The datasets and computer codes are available upon request from the authors.

Declaration of Competing Interest

The authors declare that they have no known competing financial interests or personal relationships that could have appeared to influence the work reported in this paper.

CRediT authorship contribution statement

Aleš Wodecki: Conceptualization, Methodology, Software, Validation, Formal analysis, Investigation, Data Curation, Writing - Original Draft, Writing - Review & Editing, Visualization. **Pavel Strachota:** Methodology, Software, Investigation, Writing - Original Draft, Writing - Review & Editing. **Tomáš Oberhuber:** Methodology, Writing - Review & Editing, Supervision. **Kateřina Škardová:** Methodology, Writing - Review & Editing. **Monika Balázsová**: Writing - Review & Editing.

References

1. Allen, S., Cahn, J.W.: A microscopic theory for antiphase boundary motion and its application to antiphase domain coarsening. Acta Metall. **27**, 1084–1095 (1979)
2. Alpak, F.O., Riviere, B., Frank, F.: A phase-field method for the direct simulation of two-phase flows in pore-scale media using a non-equilibrium wetting boundary condition. Computat. Geosci. **20**(5), 881–908 (2016). URL https://doi.org/10.1007/s10596-015-9551-2
3. Amiri, H.A.A., Hamouda, A.A.: Evaluation of level set and phase field methods in modeling two phase flow with viscosity contrast through dual-permeability porous medium. Int. J. Multiphase Flow **52**, 22–34 (2013)
4. Backofen, R., Ratz, A., Voigt, A.: Nucleation and growth by a phase field crystal (PFC) model. Philosophical Magazine Letters **87**(11), 813–820 (2007)
5. Beneš, M.: Anisotropic phase-field model with focused latent-heat release. In: Free Boundary Problems: Theory And Applications II, *GAKUTO International Series in Mathematical Sciences and Applications*, vol. 14, pp. 18–30 (2000)
6. Beneš, M.: Mathematical analysis of phase-field equations with numerically efficient coupling terms. Interface. Free. Bound. **3**, 201–221 (2001)
7. Beneš, M.: Mathematical and computational aspects of solidification of pure substances. Acta Math. Univ. Comenianae **70**(1), 123–151 (2001)
8. Caginalp, G.: An analysis of a phase field model of a free boundary. Arch. Rational Mech. Anal. **92**, 205–245 (1986)
9. Cahn, H.: Free energy of a nonuniform system. i. interfacial free energy. The Journal of Chemical Physics (1958)

10. Christian Miehe Lisa-Marie Schanzel, H.U.: Phase field modeling of fracture in multi-physics problems. part I. balance of crack surface and failure criteria for brittle crack propagation in thermo-elastic solids. Comput. Method. Appl. M. **294**, 449–485 (2015)

11. Chrysafinos, K., Gunzburger, M., Hou, L.: Semidiscrete approximations of optimal robin boundary control problems constrained by semilinear parabolic pde. Journal of Mathematical Analysis and Applications **323**(2), 891–912 (2006). DOI https://doi.org/10.1016/j.jmaa.2005.10.053. URL `https://www.sciencedirect.com/science/article/pii/S0022247X05010619`

12. Colli, P., Gilardi, G., Marinoschi, G., Rocca, E.: Optimal control for a conserved phase field system with a possibly singular potential. Evolution Equations & Control Theory **7**(1), 95–116 (2018)

13. Colli, P., Signori, A., Sprekels, J.: Optimal control of a phase field system modelling tumor growth with chemotaxis and singular potentials. Appl. Math. Opt. **83**, 2017–2049 (2019)

14. Conti, M., Giorgini, A., Grasselli, M.: Phase-field crystal equation with memory. J. Math. Anal. Appl. **436**(2), 1297–1331 (2015)

15. Şener, c., Subaşı, M.: On a neumann boundary control in a parabolic system. Boundary Value Problems **2015** (2015). DOI 10.1186/s13661-015-0430-5

16. Gong, W., Hinze, M., Zhou, Z.: Finite element method and a priori error estimates for dirichlet boundary control problems governed by parabolic PDEs. J. Sci. Comput. **66**(3), 941–967 (2016). DOI 10.1137/100795632

17. Gudi, T., Mallik, G., Sau, R.: Finite element analysis of the Dirichlet boundary control problem governed by linear parabolic equation. arXiv p. arXiv:2111.02039 (2021)

18. Guo, Z., Xiong, S.M.: Study of dendritic growth and coarsening using a 3-D phase field model: Implementation of the Para-AMR algorithm. IOP Conf. Ser.: Mater. Sci. Eng. **84**, 012067 (2015)

19. Hinze, M., Pinnau, R., Ulbrich, M., Ulbrich, S.: Optimization with PDE Constraints. Springer (2009)

20. Hoffman, K.H., Jiang, L.: Otimal control of a phase field model for solidification. Numerical Functional Analysis and Optimization **13**, 11–27 (1992)

21. Jeong, J.H., Goldenfeld, N., Dantzig, J.A.: Phase field model for three-dimensional dendritic growth with fluid flow. Phys. Rev. E **64**, 041602 (2001)

22. Karma, A., Rappel, W.J.: Quantitative phase-field modeling of dendritic growth in two and three dimensions. Phys. Rev. E **57**(4), 4 (1998)

23. Kobayashi, R.: Modeling and numerical simulations of dendritic crystal growth. Physica D **63**, 410–423 (1993)

24. Kunisch, K., Vexler, B.: Constrained dirichlet boundary control in l^2 for a class of evolution equations. SIAM J. Control Optim. **46**, 1726–1753 (2007). DOI 10.1137/060670110

25. Langer, J.S.: Models of pattern formation in first-order phase transitions. Directions in Condensed Matter Physics pp. 165–186 (1986)

26. Leugering, G., Engell, S., Griewank, A., Hinze, M., Rannacher, R., Schulz, V., Ulbrich, M., Ulbrich, S.: Constrained Optimization and Optimal Control for Partial Differential Equations. International Series of Numerical Mathematics. Birkhäuser (2012). DOI 10.1007/978-3-0348-0133-1

27. Strachota, P., Wodecki, A.: High resolution 3D phase field simulations of single crystal and polycrystalline solidification. Acta Phys. Pol. A **134**(3), 653–657 (2018). DOI 10.12693/APhysPolA.134.653. URL `http://przyrbwn.icm.edu.pl/APP/PDF/134/app134z3p09.pdf`

28. Strachota, P., Wodecki, A., Beneš, M.: Focusing the latent heat release in 3D phase field simulations of dendritic crystal growth. Modelling Simul. Mater. Sci. Eng. **29**, 065009 (2021)

29. Wu, J.Y., Nguyen, V.P., Nguyen, C.T., Sutula, D., Sinaie, S., Bordas, S.P.: Chapter one - phase-field modeling of fracture. pp. 1–183. Elsevier (2020). DOI https://doi.org/10.1016/bs.aams.2019.08.001. URL `https://www.sciencedirect.com/science/article/pii/S0065215619300134`

30. Zonghong, X., Wei, W., Ying, Z., Yue, W., Yumei, L.: Optimal control for a phase field model of melting arising from inductive heating. AIMS Mathematics **7(1)**, 121–142 (2022)